Article

Wind Tunnel Study on the Tip Speed Ratio's Impact on a Wind Turbine Wake Development

Ingrid Neunaber [1,2], **Michael Hölling** [3,*] **and Martin Obligado** [4,*]

1 Department of Energy and Process Engineering, Norwegian University of Science and Technology, 7034 Trondheim, Norway
2 LHEEA/CNRS, École Centrale de Nantes, 44300 Nantes, France
3 Institute of Physics and For Wind, University of Oldenburg, 26129 Oldenburg, Germany
4 CNRS, Grenoble INP, LEGI, Université Grenoble Alpes, 38000 Grenoble, France
* Correspondence: michael.hoelling@uol.de (M.H.); martin.obligado@univ-grenoble-alpes.fr (M.O.); Tel.: +49-441-798-3951 (M.H.); +33-4-76-82-50-46 (M.O.)

Abstract: We propose an experimental study on the influence of the tip speed ratio on the spatial development of a wind turbine wake. To accomplish this, a scaled wind turbine is tested in a wind tunnel, and its turbulent wake measured for streamwise distances between 1 and 30 diameters. Two different tip speed ratios (5.3 and 4.5) are tested by varying the pitch angle of the rotor blades between the optimal setting and one with an offset of $+6°$. In addition, we test two Reynolds numbers for the optimal tip speed ratio, $Re_D = 1.9 \times 10^5$ and $Re_D = 2.9 \times 10^5$ (based on the turbine diameter and the freestream velocity). For all cases, the mean streamwise velocity deficit at the centerline evolves close to a power law in the far wake, and we check the validity of the Jensen and Bastankhah-Porté-Agel engineering wind turbine wake models and the Townsend-George wake model for free shear flows for this region. Lastly, we present radial profiles of the mean streamwise velocity and test different radial models. Our results show that the lateral profile of the wake is properly fitted by a super-Gaussian curve close to the rotor, while Gaussian-like profiles adapt better in the far wake.

Keywords: wind turbine wake; wake models; experimental fluid dynamics

1. Introduction

With the strong increase in the number of wind turbines in wind farms, the demand of reliable, fast, cost-efficient wake models is growing: In a wind farm, downstream wind turbines operate (sometimes partially) in the wakes of upstream wind turbines. For downstream turbines, consequences are power losses due to the reduced velocity in the wakes and increased loads due to the additional turbulence [1,2]. A reliable prediction of the evolution of the wake, with focus on the mean velocity deficit, is therefore of interest to optimize wind farm layouts and control algorithms with the objectives of reduction of maintenance times and increase of power.

For this reason, wind turbine wakes have been subject of many numerical and experimental studies both in the laboratory under controlled conditions and in the field for several decades (see, e.g., [2–5] for reviews). It has been shown that the turbulence in the wind turbine wake is highly complex: Directly downstream of the rotor, in the near wake, the wake is characterized by the tower wake and tip and root vortices that are shed from the blades and are transported downstream on a helical path that forms a vortex sheet which blocks the entrainment of flow to the wake (e.g., [6]). Once the vortices break down, shear layers form, and higher energetic flow from outside is entrained to the wake (e.g., [6,7]). As a consequence, turbulence builds up (e.g., [8,9]). Finally, when the shear layers meet, the turbulence starts to decay and the velocity recovers. Depending on the distance from the wind turbine, the turbulence may therefore be very different. Here, the evolution of the

wind turbine wake depends on the inflow conditions and the turbine operation conditions. Turbulence in the inflow, typically present in the atmospheric boundary layer, was shown to accelerate the breakdown of the tip vortices and, thus, accelerate the recovery of the mean velocity (e.g., [2,10]).

While there are many studies that focus on the impact of the turbulence in the inflow on the evolution of the wind turbine wake, despite its relevance, little attention has been payed to the wakes of turbines operating in non-optimal conditions. Stein & Kaltenbach [11] experimentally show that the tip speed ratio (TSR) has a strong impact on the evolution of the near wake, but this impact diminishes in the far wake. Lignarolo and collaborators [6] attribute this to the variation of the breakdown of the tip vortices. Moreover, Wu and collaborators [12] investigate the wake evolution for six different tip speed ratios and find that a higher than optimal TSR results in a reduced wake velocity deficit and turbulence intensity compared to optimal or less than optimal TSR, while simultaneously providing more power than when using a less than optimal TSR. A recent study [13] investigates the evolution of the wake of a model wind turbine with respect to different turbulence intensities and length scales in the inflow, and they repeat their experiments for three different tip speed ratios with similar findings.

Overall, this illustrates the complexity of a wind turbine wake that is evolving in the atmospheric boundary layer. For wind farm layout optimization and wind farm control algorithms, there is a need to predict wake effects in a fast and cost-efficient way despite the complex nature of this problem.

Therefore, numerous models have been proposed in recent years to predict the mean velocity deficit. Several studies evaluate their accuracy using wind tunnel experiments, field measurements and numerical simulations with different results (e.g., [14–17]) . Furthermore, the structure of the near and far wake have been studied extensively (e.g., [2,3,18]).

Wind turbine wake models can usually be divided into empirical and analytical engineering wake models. Empirical wake models are formed from fitting extended data bases, while analytical wake models are derived from governing equations and basic assumptions. Mostly, they aim at describing either the mean velocity deficit or the added turbulence intensity in the wind turbine wake. Among these engineering wake models, only few were adopted and are frequently used. A prominent example of an empirical wind turbine wake model is the Aitken model [19], while well-known analytical engineering wake models are the Jensen model [20], the Frandsen wake model [21] and the Bastankhah-Porté-Agel model [22]. We introduce the Jensen and Bastankhah-Porté-Agel wake models in Section 2, and for a more complete overview of different wind turbine wake models, the reader is referred to [2,17,23,24].

In contrast, for the axisymmetric turbulent far wake of a bluff body, an analytical model exists that is derived from few, robust assumptions [25,26]. In the following, this model will be referred to as 'Townsend-George model'. Similar to engineering wind turbine wake models, this model predicts a power law dependence of the mean velocity deficit downstream of a bluff body. However, the main difference lies in the presence of a virtual origin. It has been shown that the wake of a wind turbine fulfills the requirements necessary to apply the Townsend-George model [27], and several works that apply this phenomenology to wind turbine wakes found a better fit compared to engineering wind turbine wake models [27–31].

This work aims to discuss the influence of operation conditions on the spatial development of the turbulent wake. Furthermore, we quantitatively assess their effect on different wake models. As stated above, a systematic study on the influence of different operation conditions on these quantities has not been performed yet. For that purpose, we propose a wind tunnel study on the evolution of the turbulent wake of a wind turbine operated in different operation conditions. Two different tip speed ratios are tested (4.5 and 5.3), that are produced by testing the optimal rotor blade pitch angle and an angle with an offset of $+6°$. Further, two diameter-based Reynolds numbers are investigated for the optimal TSR, $Re_D = 1.9 \times 10^5$ and $Re_D = 2.9 \times 10^5$ with $Re_D = \frac{U_\infty D}{\nu}$ (where D denotes the rotor

diameter, U_∞ is the freestream velocity, and ν is the kinematic viscosity of air). Experiments are performed with a three-bladed model wind turbine in the large wind tunnel of the University of Oldenburg. We study the average scaling laws and turbulence properties of all cases, and the performance of the analytical and two engineering models for the evolution of the mean streamwise velocity deficit. Finally, we discuss the radial velocity profiles, as they also play a key role in engineering models.

2. Wake Models

In this section, we will briefly detail the turbulent wake models for the mean streamwise velocity deficit that will be discussed in this work. While there is a large amount of models, we focus on the two engineering models that are more widely used: the Jensen model [20] and the Bastankhah-Porté-Agel model [22]. Additionally, we apply the analytical Townsend-George theory for axisymmetric, self-preserving, turbulent wakes [25,26], that has recently been shown to properly fit the wakes of wind turbines [13,27,30,31].

2.1. Jensen Wake Model

Proposed by N.O. Jensen in 1983, the Jensen wake model is the pioneering engineering model for wind turbine wakes [20]. Derived by assuming conservation of mass and a top-hat shaped velocity deficit, the normalized velocity deficit is given by

$$\frac{\Delta U}{U_\infty} = \frac{1 - \sqrt{1 - c_T}}{(1 + 2k_j x/D)^2},\tag{1}$$

where $\Delta U = U_\infty - U_0$ is the mean centerline velocity deficit at the downstream position x, and U_0 is the mean centerline velocity. c_T is the turbine's thrust coefficient. The wake growth rate k_j assumes a linear expansion of the wake. Commonly, onshore, $k_j = 0.075$ is suggested whereas offshore, where the wake recovery is slower due to lower turbulence levels, $k_j = 0.04$ or $k_j = 0.05$ is assumed [23,32].

Here, we treat k_j as a fitting parameter, and we also explore the possibility of replacing x with $x - x_0$ (where x_0 is also a fitting parameter), thus adding a virtual origin. We would like to note that we use the original version of the Jensen wake model, although there are also several improvements to the original model, see, e.g., [14].

2.2. Bastankhah–Porté-Agel Wake Model

The Bastankhah–Porté-Agel wind turbine wake model [22] is derived from conservation of mass and momentum and it describes the three-dimensional far wake assuming a Gaussian shape of the normalized velocity deficit with respect to the hub height (i.e., $y = 0$, $z = 0$ denotes the center of the rotor as indicated also in Section 3),

$$\frac{\Delta U}{U_\infty} = \underbrace{\left(1 - \sqrt{1 - \frac{c_T}{8\left(k_{BP} \cdot x/D + 0.2\sqrt{\beta}\right)^2}}\right)}_{\text{centerline velocity deficit}} \cdot \underbrace{\exp\left(-\frac{(z/D)^2 + (y/D)^2}{2\left(k_{BP} \cdot x/D + 0.2\sqrt{\beta}\right)^2}\right)}_{\text{Gaussian velocity profile}},\tag{2}$$

with

$$\beta = \frac{1 + \sqrt{1 - c_T}}{2\sqrt{1 - c_T}}.\tag{3}$$

Here, k_{BP} is an adaptable parameter, and y and z are the span-wise and wall-normal coordinates, respectively. Again, we will additionally explore the possibility of replacing x with $x - x_0$.

2.3. Townsend-George Model for Free Shear Flows

A.A.Townsend [33] and W.K.George [26] derived the evolution of, among other quantities, the normalized mean velocity deficit of the far wake of a bluff body assuming self-

similarity of the one-point turbulence quantities and high-Reynolds number turbulence with a decay according to the Kolmogorov phenomenology [34],

$$\Delta U(x) = A_{TG} U_\infty ((x - x_0)/\theta)^{-2/3}, \tag{4}$$

A_{TG} is a scaling parameter that we will tune here. Contrary to the Jensen and Bastankhah-Porté-Agel models, x_0 is native to this model. This model also incorporates the prediction of the evolution of the wake width $\delta(x) \propto (x - x_0)^{1/3}$. The momentum thickness, constant over x, is defined as,

$$\theta^2 = \frac{1}{U_\infty^2} \int_0^\infty U_\infty (U_\infty - U) y \, dy, \tag{5}$$

assuming axisymmetry. $U(x,y)$ is the mean, y-dependent, streamwise velocity.

Furthermore, it has been found that, depending on the nature of the energy cascade, the exponent $-2/3$ [35–37] may change, and exponents between $-2/3$ and -1 have been reported (that also imply a change on the exponent for δ) [35–37]. We will therefore fit our data set using the more general scaling:

$$\Delta U(x) = A_{TG} U_\infty ((x - x_0)/\theta)^\alpha, \tag{6}$$

with α the aforementioned exponent that will be taken as a fitting parameter.

2.4. Radial Velocity Profile Predictions

We will also examine predictions of the radial velocity profile, which will be discussed qualitatively in Section 4.3. As explained in the previous sections, the models propose, alternatively, a top-hat shaped profile, a Gaussian profile, or an extended Gaussian profile. In addition, it has recently been proposed that a super-Gaussian profile (defined as a modified Gaussian where the exponent within the exponential can be variable and bigger than 2) can provide better fits of the near wake of a turbine [38]. We will therefore also discuss this functional form in Section 4.3, that is not assumed by any of the three models we describe in this section.

A Gaussian velocity profile is given for the normalized mean velocity,

$$\frac{U_\infty - U(x, y/\delta)}{U_\infty - U_0} = a \cdot \exp\left(-b \cdot (y/\delta)^2\right), \tag{7}$$

where $U(x, y/\delta)$ denotes the radial velocity and the span-wise coordinate y is normalized by the wake width δ. a and b are fit parameters.

In addition, the modified constant eddy viscosity model, referred to as "extended Gaussian" profile and discussed in [39], is applied,

$$\frac{U_\infty - U(x, y/\delta)}{U_\infty - U_0} = a \cdot \exp\left(-b \cdot (y/\delta)^2 - c \cdot (y/\delta)^4 - d \cdot (y/\delta)^6\right), \tag{8}$$

where a, b, c and d are fit parameters.

Lastly, the super-Gaussian profile is given by,

$$\frac{U_\infty - U(x, y/\delta)}{U_\infty - U_0} = a \cdot \exp\left(-b \cdot (y/\delta)^n\right), \tag{9}$$

a, b and n being fitting parameters. The exponent n is expected to be larger than 2 [38].
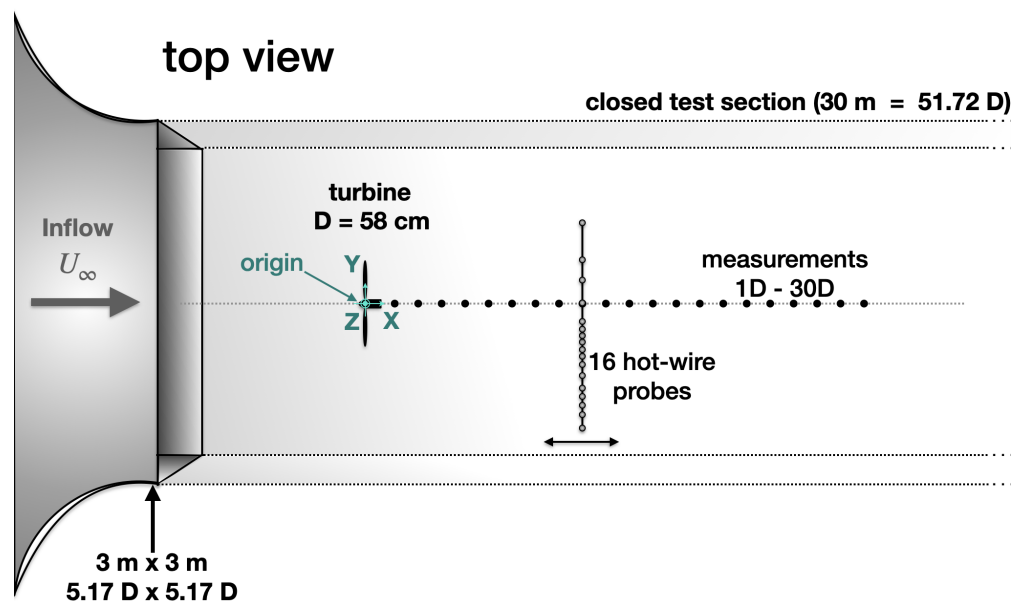
3. Experimental Setup

The measurements presented here were carried out in the wind tunnel of the University of Oldenburg. The closed-loop wind tunnel has a test section with a length of 30 m and a square cross section of $3 \times 3 \, \text{m}^2$ [40]. The maximum velocity attainable when the wind tunnel is empty is $42 \, \text{ms}^{-1}$, and the background turbulence intensity is around 0.3%. The ceiling of the wind tunnel is adjusted to avoid a speed-up of the flow downstream

in the test section (and therefore a pressure gradient in the streamwise direction). All experiments reported here were carried out in low-turbulence conditions (i.e., $TI = 0.3\%$: no grids or other turbulence generators were placed upstream the scaled wind turbine).

A single three-bladed horizontal axis model wind turbine of type MoWiTO 0.6 (cf. [41]) was mounted in the test section as illustrated in Figure 1. The model wind turbine has a hub height (when placed on a platform) of 93 cm and a rotor diameter of 58 cm. The turbine is controlled to optimize the power for a given blade pitch angle and incoming velocity. For this, a closed-loop control run by a NI cRIO-9074 real-time system with a sampling time of 5×10^{-3} s is used to keep the optimal torque of the generator. The origin of the coordinate system used here is at the center of the turbine rotor as indicated in Figure 1.

An array consisting of 16 single wire probes was used to scan the wake at hub-height (i.e., $z = 0$) between $x/D = 1$ and $x/D = 30$ in steps of $1D$. In the span-wise direction, the probes cover a range from $y/D = -1.04$ to $y/D = 1.91$. The probes are not spaced equidistantly but, as presented in Figure 2, focusing on one side of the wake, with a high probe density around the radius of the turbine ($y/D \approx -0.5 \pm 0.25$).

The hot wire placed at the centerline ($y = z = 0$) was operated using a StreamLine 9091N0102 frame with a 91C10 CTA (Constant Temperature Anemometry) Module. It was sampled at $f_s = 20$ kHz; a hardware low-pass filter with a cut-off frequency of $f = 10$ kHz was set. All other hot-wires were operated by several Dantec Dynamics *multichannel CTA* 54N80. The sampling frequency was $f_s = 6$ kHz and a hardware low-pass filter with a cut-off frequency of $f = 3$ kHz was used. Data was collected synchronized using two NI USB 6211 A/D converters, and the sampling time was 240 s. The hot wires were calibrated frequently, at least twice a day.

Figure 1. Experimental Setup: A model wind turbine is installed in the wind tunnel of the University of Oldenburg. The wake is measured with a horizontal array of 16 hot-wire probes in the range $1D$ to $30D$ downstream of the wind turbine. The positions of the hot-wires are indicated in Figure 2.

Three operating configurations were studied. For the first one, the turbine is operated with an incoming velocity of $U_\infty = 7.5$ m/s (and therefore $Re_D = 2.9 \times 10^5$). At this inflow velocity, the turbine model used operates at the optimal tip-speed ratio ($TSR_o = 5.3$) and thrust force if the pitch angle of the rotor blades γ_o is the optimal pitch angle. The operation and inflow conditions are similar to experiments performed with the same model wind turbine in [27,42,43]. The second configuration consists of the same freestream velocity but using a different, non-optimal blade pitch angle of $\gamma_{no} = \gamma_o + 6°$, and, thus, a non-optimal TSR of 4.5. Finally, for the third configuration, a lower velocity, $U_\infty = 5.0$ ms^{-1} ($Re_D = 1.9 \times 10^5$), is investigated at optimal TSR and γ_o (allowing to test partial load

conditions). The main properties of each case are detailed in Table 1. This setup therefore allows us to test cases with approximately equal TSR but different Re_D.
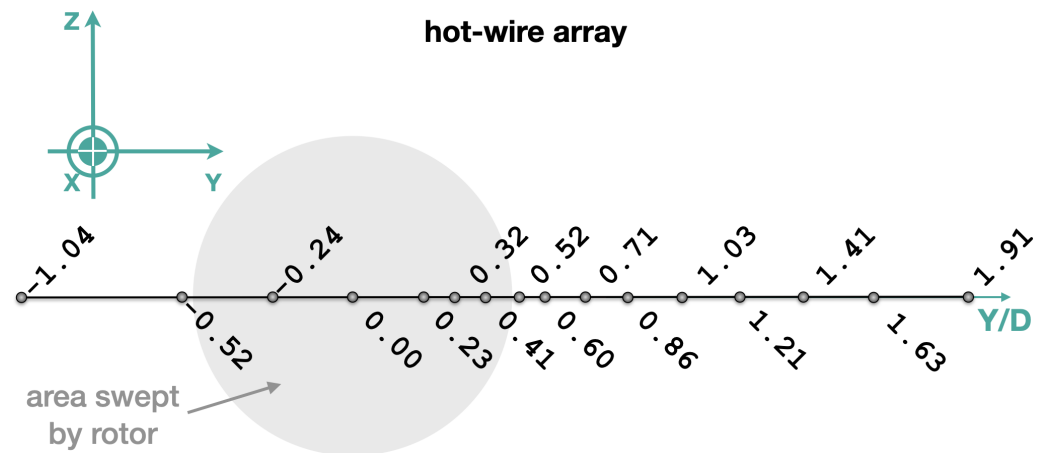

Figure 2. Positions of the hot-wires mounted on the hot-wire array shown in Figure 1.

Table 1. Parameters for the three cases studied: freestream velocity (U_∞), rotor-based Reynolds number, blade pitch angle γ with respect to the optimal pitch angle γ_o, thrust coefficient c_T, total thrust of the turbine, and TSR.

Case	U_∞ (m/s)	Re_D	γ	c_T	Thrust (N)	TSR
1	7.5	$Re_D = 2.9 \times 10^5$	γ_o	0.70	6.37	5.31
2	7.5	$Re_D = 2.9 \times 10^5$	$\gamma_o + 6°$	0.34	3.44	4.53
3	5.0	$Re_D = 1.9 \times 10^5$	γ_o	0.73	2.95	5.25

4. Results

### 4.1. Mean Streamwise Quantities

We first study the streamwise evolution of the normalized centerline velocity deficit $(U_\infty - U_0)/U_\infty$ (Figure 3a) for the three cases. It can be observed that the velocity deficits of all cases are very different close to the rotor ($x/D \leq 12$). In the far wake, case 1 experiences a better recovery, while cases 2 & 3 collapse onto a single curve. This is an interesting finding, as it shows that the recovery is depending on the TSR but also on Re_D.

Next, we investigate the evolution of the wake width δ for the three cases (Figure 3b) to better describe the spatial evolution of the wake. This parameter is defined as [26]

$$\delta^2(x) = \frac{1}{U_0} \int_0^\infty (U_\infty - U(x,y))y\,dy, \tag{10}$$

where, as for the momentum thickness θ, $U(x,y)$ is the mean, y-dependent, streamwise velocity, and axisymmetry is assumed. In the near wake, wind turbines are observed to produce an accelerated 'ring' just outside the rotor swept area with negative velocity deficit, see Figure 6 (cf. also, e.g., Figure 15 in [44] or Figure 11 in [6]). To calculate the wake width, for values of $U(x,y)$ where an acceleration is observed, the velocity deficit was set to zero in Equation (10). This phenomenon arises only in the near wake, and is not significant for $x/D > 5$. Finally, given that the curves are smooth but discretized (see Figure 7), the values were linearly interpolated into a 1024 grid to increase the accuracy of the integral.

Figure 3b shows that, as expected, δ increases for all cases. Moreover, for $x/D \geq 5$, cases 1 and 3 have very similar values of δ, while case 2 has a value around 15% lower. Overall, the evolution of δ and the normalized centerline velocity deficit suggest that the turbulent wake has a different streamwise evolution when the value of the TSR is modified by varying the blade pitch angle.
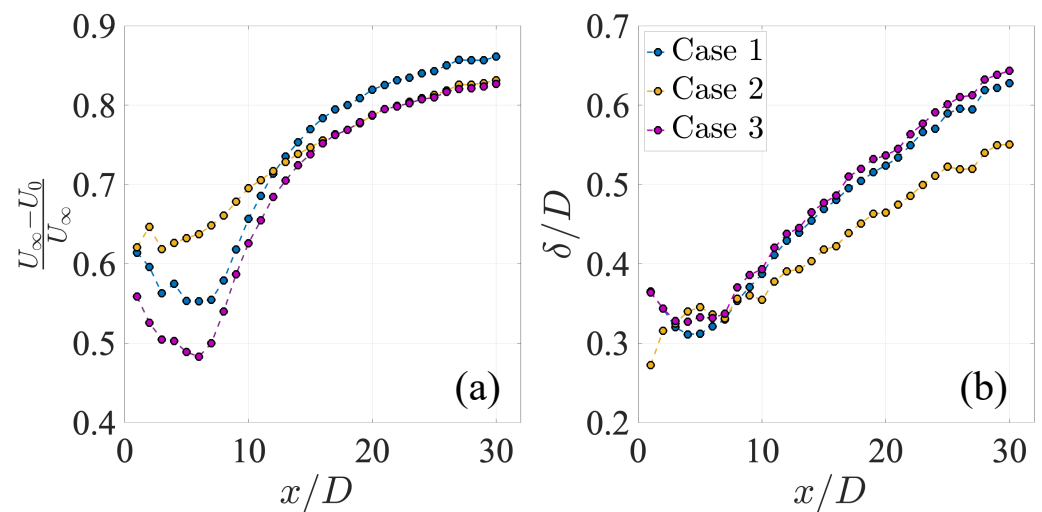
Figure 3. Streamwise profiles of the mean velocity deficit (**a**) and wake width δ (**b**) for the three cases.

To further explore the differences in the wake properties for the three cases, in Figure 4, we show the streamwise evolution of different turbulence parameters. To guarantee proper temporal resolution for computing these parameters, we analyze only the centerline values, that were acquired with a sampling frequency of $f_s = 20$ kHz. The turbulence intensity, defined as the ratio between the standard deviation of the streamwise velocity $\sigma_{u(t)}$ and the mean centerline velocity $U_0(x)$, peaks for all cases at $x/D = 8$ (Figure 4a). However, a clear dependence of the downstream evolution of the turbulence intensity on the TSR is visible. Case 3 produces the largest turbulence intensities. Case 1 has smaller values but shows the same behavior. Remarkably, in case 2, the turbulence intensity in the wake is very low, and an overall dampened evolution is apparent, a trend that is also observed in [12] for TSRs significantly lower than the optimal TSR (note that the TSR is varied in [12] by varying the generator load and not the blade pitch angle). A similar behavior is observed for the turbulent Reynolds number Re_λ (defined as $Re_\lambda = \sigma_{u(t)}\lambda/\nu$, with λ denoting the Taylor micro scale), where case 1 has values almost twice that of the other ones. Furthermore, case 1 and 3 present a decay of turbulence in the far wake while case 2 still shows a small increase of the Taylor Reynolds number (Figure 4b). Nevertheless, such trends are small, and new experiments testing this quantity further downstream could confirm them. Finally, the integral length scale L_{int} (defined using the first zero-crossing of the autocorrelation [45,46]) has the same trend for all three cases, increasing with x to scales similar to the rotor radius (where $L_{int}^{Case1} > L_{int}^{Case3} > L_{int}^{Case2}$).

Overall, the streamwise evolution of the centerline velocity deficit, δ, and other turbulence parameters suggest that cases 1 and 3, that have approximately the same TSR, produce a well-developed flow, showing the standard properties of decaying turbulence in the far wake [27]. Nevertheless, they do present some relevant differences for the wake recovery and values of Re_λ in the centerline. In contrast, case 2 presents several differences (notably, the increase of Re_λ with increasing downstream position) that point towards the possibility that the flow is still not completely developed, and even at $x/D = 30$, the turbulent flow is not yet freely decaying. A possible transition for turbulence parameters may be present at $x/D = 15$ for this case, as the trends of all curves are slightly altered. This may be related to production of turbulence due to the mixing of coherent structures, or the lack of axisymmetry of the wake. Future experiments visualizing the flow in 2D or 3D may help to explain this phenomenon.
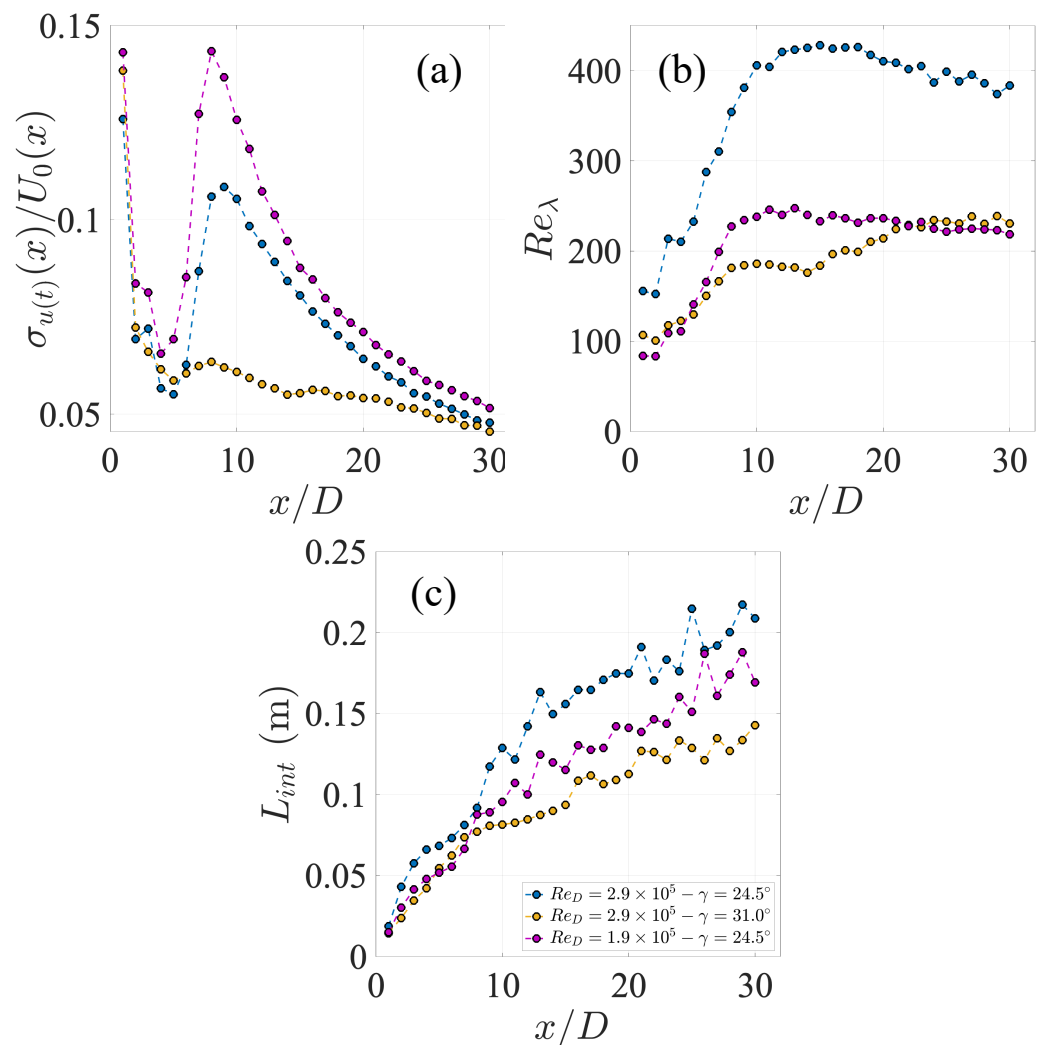
Figure 4. Streamwise evolution of turbulence properties for all cases: turbulence intensity $\sigma_{u(t)}(x)/U_0(x)$ (**a**), Taylor-scale-based Reynolds number Re_λ (**b**), and integral length scale L_{int} (**c**).

4.2. Application of Wake Models

Figures 5a–c show the fits of the normalized centerline velocity deficit $(U_\infty - U_0)/U_\infty$ using the wake models described in Section 2. All the fitting parameters can be found in Table 2, and the accuracy based on the root mean square fitting errors are given in Table 4. The fits were applied downstream between $8D$ and $30D$, where the turbulence intensity is decaying for all three cases.

It can be observed that the Townsend-George fit performs best for all three cases, while the Bastankhah-Porté-Agel wake model still captures the decay of the wake reasonably well. We remark that the Townsend-George model is the only one designed specifically for the far wake, and it is therefore expected that it will work better in the range $8D < x < 30D$ [27]. We would also like to note that the latter model was applied, on a first instance, by setting the virtual origin to zero.

Since the addition of a virtual origin was shown to significantly increase the performance of all available models [27,30,31], we show in Figure 5d–f the same fits as in the previous case but with a virtual origin added for all cases. For this case, all the fitting parameters can be found in Table 3 and the root mean square fitting errors are also reported in Table 4 (where the fits were, once more, applied between $8D$ and $30D$).
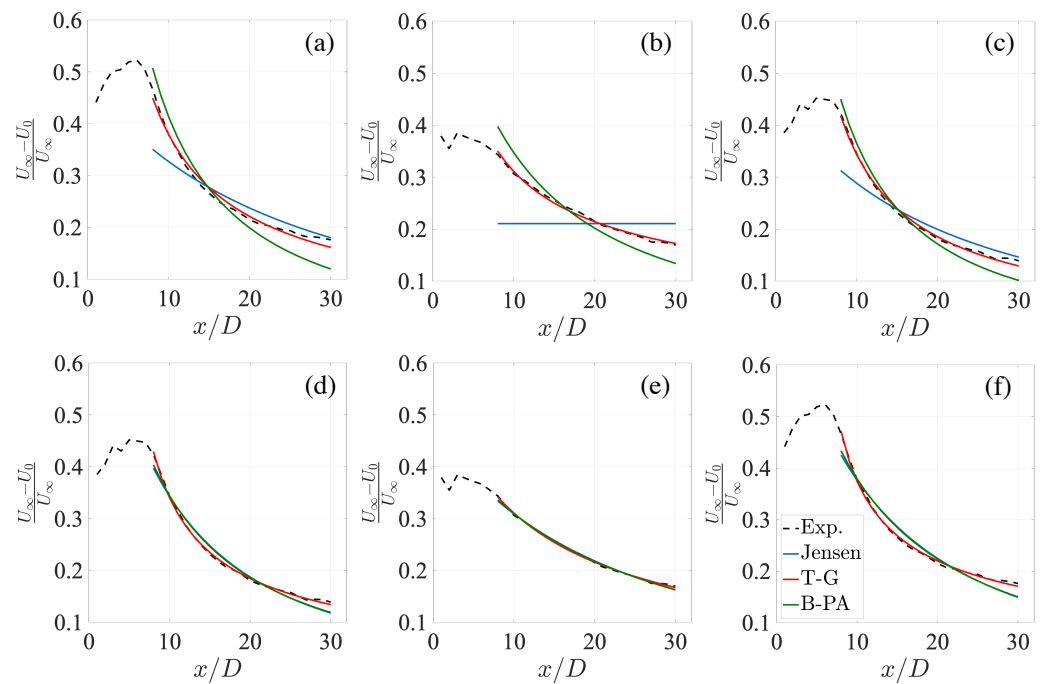
Figure 5. Streamwise evolution of the normalized mean velocity deficit with the wake model fits. The first column shows results for case 1 (**a,d**), the second for case 2 (**b,e**), and the third for case 3 (**c,f**). The first row (**a–c**) shows fits with no virtual origin and the second row (**d–f**) shows fits where a virtual origin was added.

Table 2. Fit parameters for the wake models as shown in Figure 5 for the application without virtual origin. $B - PA$ stands for Bastankhah-Porté-Agel and $T - G$ for Townsend-George.

Case	Jensen	B-PA	T-G	
	k_j	k_{BP}	A_{TG}	α
1	0.0126	0.0145	2.65	−0.89
2	2.6×10^{-7}	0.0074	1.07	−0.55
3	0.0105	0.0131	2.25	−0.77

Table 3. Fit parameters for the wake models as shown in Figure 5. A virtual origin is included.

Case	Jensen		B-PA		T-G		
	k_j	x_0	k_{BP}	x_0	A_{TG}	α	x_0
1	0.02	6.35	0.012	−3.21	1.3	−0.69	3.03
2	0.0078	21.14	0.0048	−7.99	4.28	−0.88	−9.61
3	0.0166	6.17	0.0094	−5.25	4.53	−0.89	−0.51

A significant improvement is observed for all models, where the Townsend-George model is always the better performing one. Nevertheless, the root mean square error indicates that all wake models perform appropriately for the test cases.

Table 4. Fit accuracy in % for the fits shown in Figure 5. The columns labelled with a 'VO' correspond to values where a virtual origin was added.

Case	Jensen	Jensen VO	B-PA	B-PA VO	T-G	T-G VO
1	93.9	97.5	99.3	98.1	99.5	99.8
2	95.7	99.5	99.8	99.6	99.4	99.9
3	91.7	95.4	98.8	96.3	98.8	99.8

To conclude this section, we remark that all fitting parameters seem to be strongly affected by the TSR. Although the Jensen and Bastankhah-Porté-Agel models include the value of c_T in their formulæ, the fit parameters show strong variations with respect to the TSR. Moreover, some differences are also present between cases 1 and 3, suggesting that Re_D (within the somewhat moderate range explored in this work) is also playing a role on the applicability of the models.

4.3. Radial Profiles

We now focus on the radial profiles of the normalized velocity deficit, cf. Figure 6, to explore the impact that a variation of operation conditions has on the span-wise wake evolution. We first note that pointed profiles are observed at the centerline for large values of x in cases 2 and 3, showing the presence of strong gradients of the streamwise velocity. It should be noted that they are also partially due to a lack of resolution around the centerline ($y = 0$). Indeed, given the probe spacing on the array, there is a gap of $0.24D$ around the centerline. Nevertheless, plots of isolated profiles (see Figure 7) show that their shape is appropriately resolved. Finally, small local peaks present for some values of y are caused by small deviations in the calibration performance among hot wires.
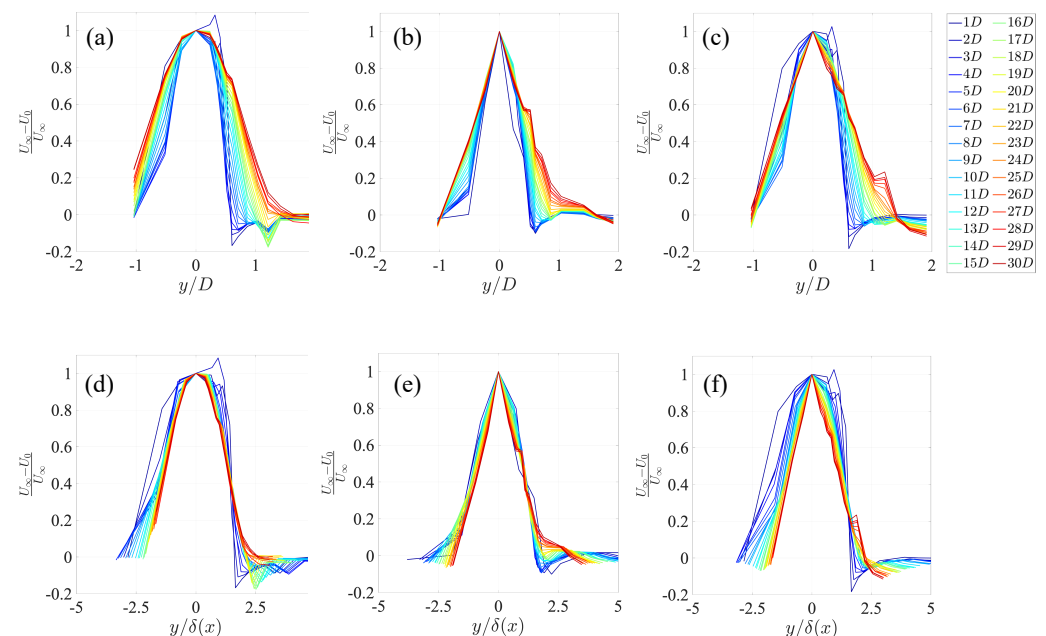

Figure 6. Horizontal profiles of the self-similar function $f(\eta) = \frac{U_\infty - U_0}{U_\infty}$ for all streamwise distances covered. In the first row (**a**–**c**), the horizontal coordinate y has been normalized with D, while in the second row (**d**–**f**), the horizontal coordinate y has been normalized with $\delta(x)$. The first column (**a**,**d**) shows results for case 1, the second (**b**,**e**) for case 2, and the third (c,f) for case 3.

Overall, the difference in the wake shape and size becomes evident (Figure 6a–c), where, consistently with the findings from Figure 3a, case 1 produces the largest wake. Furthermore, in the far wake (starting from around $x/D \approx 15$), all curves collapse when normalized by δ (Figure 6d–f). This suggest that velocity deficit has already become self-similar in that region. This observation is relevant, as several wake models and theoretical developments rely on such hypothesis.

We now check different fits of the radial profiles. As discussed in Section 2, the models alternatively propose a top-hat shaped velocity profile, a Gaussian profile, an extended Gaussian profile, or a super-Gaussian profile. We therefore fit the last three functions for one position in the near wake ($5D$), one in the transition region ($10D$), and two within the far wake (20 and $30D$). As the fit parameters for the radial fits are not always defined by means of available quantities, we limit our analysis to a qualitative study. We note that

negative values of the velocity deficit observed (mostly at $5D$) were, once more, ignored for the fits (more precisely, the velocity deficit was set to zero). Attempts to model such cases via Ricker wavelets were not successful.
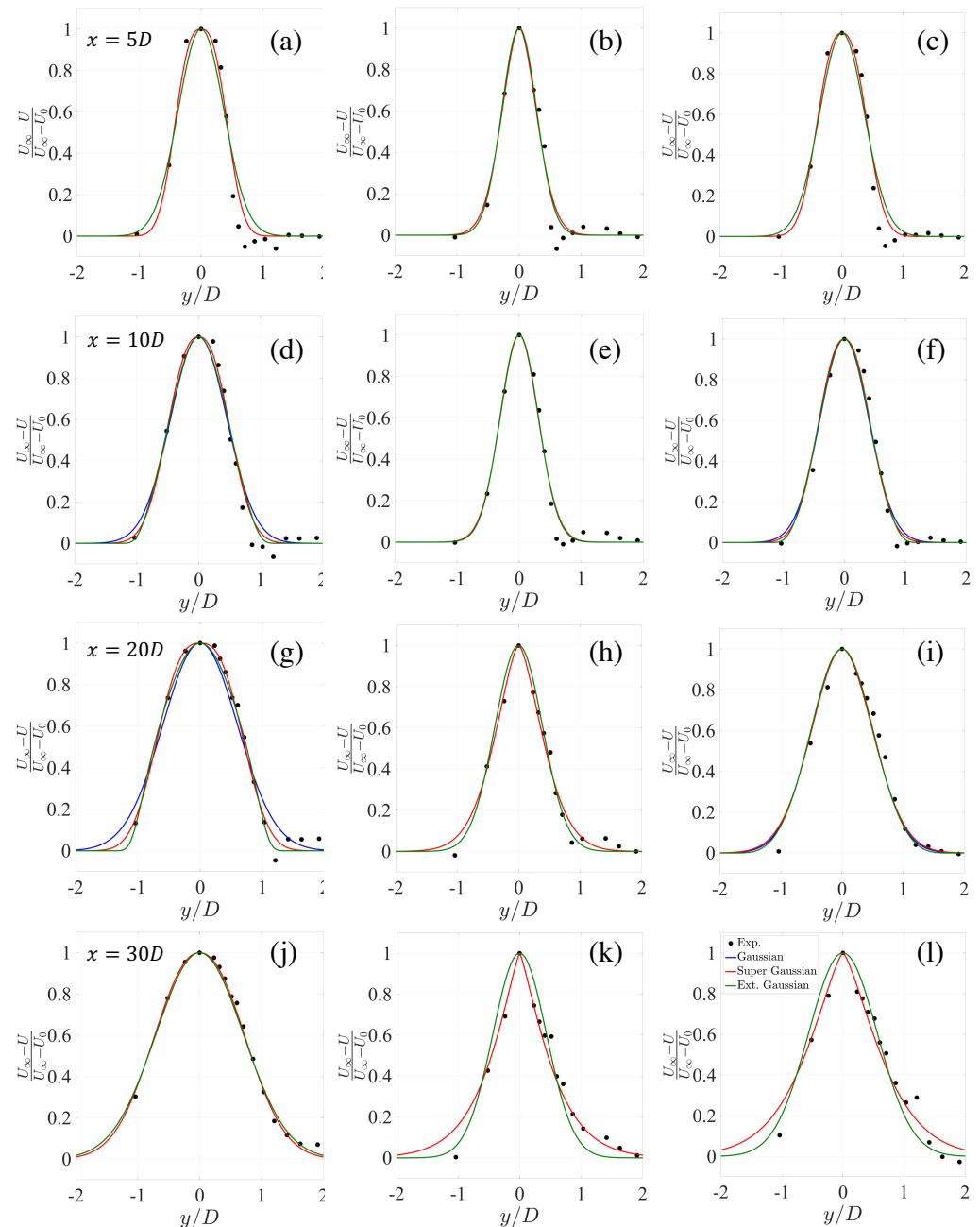
Figure 7. Horizontal profiles at 5 (first row: **a–c**), 10 (second row: **d–f**), 20 (third row: **g–i**), and 30 (fourth row: **j–l**) diameters downstream. The first column (**a,d,g,j**) shows results for case 1, the second (**b,e,h,k**) for case 2, and the third (**c,f,i,l**) for case 3. Note that some of the fits collapse.

For case 1, the super-Gaussian fit performs best at $x = 5D$, with an exponent of $n = 2.66$. Far away, all three fits give similar results, the super-Gaussian curve has an exponent of $n = 2.16$ at $30D$, and the Gaussian and the extended Gaussian curves collapse onto a single one.

For case 2, the three fits perform similar with the exception of $30D$. At $5D$, the super-Gaussian fit exponent is $n = 1.80$ while the exponent at $30D$ is $n = 1.24$, which is somewhat unphysical. Still, for this distance, the super-Gaussian fit captures the pronounced peak at

the centerline. A similar trend is found for case 3, with a super-Gaussian whose fit exponent decreases from $n = 2.4$ at $5D$ to $n = 1.4$ at $30D$.

In conclusion, for case 1, where the shape of the wake is properly captured, our measurements show the expected behavior, and the super-Gaussian profile performs better than the other profiles in the near wake, giving place to Gaussian-like shapes in the far wake. Cases 2 and 3 show a suggestive difference. The fact that Gaussian fits do not perform well at all streamwise distances suggests that the wake shape may be significantly affected by variations of the operation conditions, but the limitations of our experimental setup do not allow us to draw any conclusions on this point. Further studies on similar working conditions for wind turbine wakes may help to shed light on this point.

5. Discussion and Conclusions

This work addresses the influence of the tip speed ratio and the Reynolds number on the spatial evolution of an axisymmetric turbulent wind turbine wake. A wind tunnel experiment with a model wind turbine was used to study the evolution of the wake from 1 to 30 diameters downstream. A hot-wire array was used to capture the centerline statistics and the time-averaged radial shape of the turbulent wake.

Three cases were studied, that involve two different tip speed ratios and two different Reynolds numbers.

We find that the operation conditions have a strong influence on several averaged properties of the wake. For the turbine within optimal conditions (in terms of TSR and thrust force), both the velocity deficit and the wake width are the largest (the latter being similar to case 3, with a similar TSR and c_T but different Reynolds number). This is indeed consistent with the underlying physics, as the energy extracted from the incoming flow will be equal to the kinetic energy deficit between the global wake and the base flow. Finally, case 2, where the turbine works at a non-optimal TSR, presents significant differences, as it generates both the smallest velocity deficits and the smallest wake width. This study is unique as it allows to quantify such differences. Concerning the applicability of wake models, we find that, within the far wake, the Townsend-George model for free shear flows performs better than two engineering wind turbine wake models. Nevertheless, as found previously in other works, the addition of a virtual origin significantly improves the performance of all available models. Furthermore, the mean radial profile of the near wake is well fitted by a super-Gaussian profile, while the far wake recovers to a Gaussian-like shape.

Further, we also find an important dependency of the evolution of the centerline turbulence on the operating conditions. Case 1 generates the most turbulent flow with Reynolds numbers Re_λ almost twice as large as for the other cases. However, in case 2, the largest values of the turbulence intensity are found. In contrast, in case 3, the turbulence does not seem to be fully developed, presenting anomalous trends such as low turbulence intensity and possible changes of the turbulence regime. These findings are relevant because, on the one hand, they are helpful to validate several turbulence models used in numerical simulations. On the other hand, they are also related to several unsteady dynamics in wind energy applications, such as blades' vibration and energy output fluctuations, among others.

Lastly, we confirm that the tip speed ratio significantly modifies the average streamwise scalings and properties of the turbulent flow, and we also find non-negligible variations of the wake at constant tip speed ratio but varying Reynolds number. Our results suggest the necessity to conduct further experiments where such tuning is possible. Overall, this work provides quantitative evidence of the influence of the TSR, c_T and Reynolds number on the spatial evolution of the wake. In particular, it is clearly shown how the wake models that predict the streamwise and radial averaged velocity deficits need to be adapted to account for these parameters.

This work also leaves some open questions that can be addressed in further research. For instance, the use of a hot-wire rake severely limits the characterization of the near wake, where the flow did not become axisymmetric nor self-similar yet, while our results

show that several properties in the near wake are strongly dependent on the operation conditions. Three-dimensional visualisation would allow to better characterise this area of the flow. Furthermore, our study is limited to non-turbulent inflows with a freestream velocity parallel to the turbine's axis. The experimental setup can therefore be expanded to include more realistic conditions by adding background turbulence and a yaw angle between the turbine and the freestream flow.

Abbreviations

The following abbreviations are used in this manuscript:

TSR	Tip speed ratio
$B - PA$	Bastankhah-Porté-Agel
$T - G$	Townsend George
D	Turbine's diameter
U_∞	Free-stream velocity
Re_D	Reynolds number based based on U_∞ and D.
Re_λ	Turbulent Reynolds number
U_0	Averaged streamwise velocity at the centerline
U	Radial averaged streamwise velocity
L_{int}	Integral length scale of the fluctuating streamwise velocity
$\sigma_{u(t)}$	RMS value of the fluctuating streamwise velocity

References

1. Barthelmie, R.J.; Frandsen, S.T.; Nielsen, M.N.; Pryor, S.C.; Rethore, P.E.; Jørgensen, H.E. Modelling and Measurements of Power Losses and Turbulence Intensity in Wind Turbine Wakes at Middelgrunden Offshore Wind Farm. *Wind Energy* **2007**, *10*, 517–528. [CrossRef]
2. Porté-Agel, F.; Bastankhah, M.; Shamsoddin, S. Wind-Turbine and Wind-Farm Flows: A Review. *Bound.-Layer Meteorol.* **2020**, *174*, 1–59. [CrossRef]
3. Vermeer, L.; Sørensen, J.; Crespo, A. Wind turbine wake aerodynamics. *Prog. Aerosp. Sci.* **2003**, *39*, 467–510. [CrossRef]
4. Stevens, R.J.; Meneveau, C. Flow structure and turbulence in wind farms. *Annu. Rev. Fluid Mech.* **2017**, *49*, 311–339. [CrossRef]
5. Neunaber, I. Turbulence of Wakes. In *Handbook of Wind Energy Aerodynamics*; Stoevesandt, B., Schepers, G., Fuglsang, P., Yuping, S., Eds.; Springer International Publishing: Cham, Switzerland, 2020; pp. 1–34._45-1. [CrossRef]
6. Lignarolo, L.; Ragni, D.; Krishnaswami, C.; Chen, Q.; Simão Ferreira, C.; van Bussel, G. Experimental analysis of the wake of a horizontal-axis wind-turbine model. *Renew. Energy* **2014**, *70*, 31–46.
7. Hamilton, N.M.; Tutkun, M.; Cal, R.B., Turbulent and Deterministic Stresses in the Near Wake of a Wind Turbine Array. In *Whither Turbulence and Big Data in the 21st Century?* Pollard, A.; Castillo, L.; Danaila, L.; Glauser, M., Eds.; Springer International Publishing: Berlin/Heidelberg, Germany, 2017.

8. Kermani, N.A.; Andersen, S.; Sørensen, J.; Shen, W. Analysis of turbulent wake behind a wind turbine. In Proceedings of the 2013 International Conference on Aerodynamics of Offshore Wind Energy Systems and Wakes, Lyngby, Denmark, 17–19 June 2013.

9. Neunaber, I.; Hölling, M.; Stevens, R.; Schepers, G.; Peinke, J. Distinct Turbulent Regions in the Wake of a Wind Turbine and Their Inflow-Dependent Locations: The Creation of a Wake Map. *Energies* **2020**, *13*, 5392. [CrossRef]

10. Aubrun, S.; Loyer, S.; Hancock, P.; Hayden, P. Wind turbine wake properties: Comparison between a non-rotating simplified wind turbine model and a rotating model. *J. Wind Eng. Ind. Aerodyn.* **2013**, *120*, 1–8. [CrossRef]

11. Stein, V.P.; Kaltenbach, H.J. Wind-tunnel modelling of the tip-speed ratio influence on the wake evolution. *J. Phys. Conf. Ser.* **2016**, *753*, 032061. [CrossRef]

12. Wu, Y.T.; Lin, C.Y.; Hsu, C.M. An Experimental Investigation of Wake Characteristics and Power Generation Efficiency of a Small Wind Turbine under Different Tip Speed Ratios. *Energies* **2020**, *13*, 2113. [CrossRef]

13. Gambuzza, S.; Ganapathisubramani, B. The influence of freestream turbulence on the development of a wind turbine wake. *arXiv* **2022**, arXiv:2209.06627.

14. Campagnolo, F.; Molder, A.; Schreiber, J.; Bottasso, C.L. Comparison of Analytical Wake Models with Wind Tunnel Data. *J. Phys. Conf. Ser.* **2019**, *1256*, 012006. [CrossRef]

15. Lopes, A.M.; Vicente, A.H.; Sánchez, O.H.; Daus, R.; Koch, H. Operation assessment of analytical wind turbine wake models. *J. Wind Eng. Ind. Aerodyn.* **2022**, *220*, 104840. [CrossRef]

16. Jeon, S.; Kim, B.; Huh, J. Comparison and verification of wake models in an onshore wind farm considering single wake condition of the 2 MW wind turbine. *Energy* **2015**, *93*, 1769–1777. [CrossRef]

17. Hegazy, A.; Blondel, F.; Cathelain, M.; Aubrun, S. LiDAR and SCADA data processing for interacting wind turbine wakes with comparison to analytical wake models. *Renew. Energy* **2022**, *181*, 457–471. [CrossRef]

18. Ivanell, S. Wake Structures. In *Handbook of Wind Energy Aerodynamics*; Stoevesandt, B., Schepers, G., Fuglsang, P., Yuping, S., Eds.; Springer International Publishing: Cham, Switzerland, 2020; pp. 1–12. [CrossRef]

19. Aitken, M.L.; Banta, R.M.; Pichugina, Y.L.; Lundquist, J.K. Quantifying Wind Turbine Wake Characteristics from Scanning Remote Sensor Data. *J. Atmos. Ocean. Technol.* **2014**, *31*, 765–787. [CrossRef]

20. Jensen, N.O. *A Note on Wind Generator Interaction*; Technical Report; Risø National Laboratory: Roskilde, Denmark, 1983.

21. Frandsen, S.; Barthelmie, R.; Pryor, S.; Rathmann, O.; Larsen, S.; Højstrup, J.; Thøgersen, M. Analytical modelling of wind speed deficit in large offshore wind farms. *Wind Energy* **2006**, *9*, 39–53. [CrossRef]

22. Bastankhah, M.; Porté-Agel, F. A new analytical model for wind-turbine wakes. *Renew. Energy* **2014**, *70*, 116–123. [CrossRef]

23. Göçmen, T.; van der Laan, P.; Réthoré, P.E.; na Diaz, A.P.; Larsen, G.C.; Ott, S. Wind turbine wake models developed at the technical university of Denmark: A review. *Renew. Sustain. Energy Rev.* **2016**, *60*, 752–769. [CrossRef]

24. Schmidt, J.; Vollmer, L. Industrial Wake Models. In *Handbook of Wind Energy Aerodynamics*; Stoevesandt, B., Schepers, G., Fuglsang, P., Yuping, S., Eds.; Springer International Publishing: Cham, Switzerland, 2020; pp. 1–28.

25. Townsend, A. *The Structure of Turbulent Shear Flow*; Cambridge University Press: Cambridge, UK, 1976.

26. George, W. The self-preservation of turbulent flows and its relation to initial conditions and coherent structures. In *Advances in Turbulence*; George, W., Arndt, R., Eds.; Springer: Berlin/Heidelberg, Germany, 1989.

27. Neunaber, I.; Peinke, J.; Obligado, M. Application of the Townsend–George theory for free shear flows to single and double wind turbine wakes—A wind tunnel study. *Wind. Energy Sci.* **2022**, *7*, 201–219. [CrossRef]

28. Okulov, V.; Naumov, I.; Mikkelsen, R.F.; Sørensen, J.N. Wake effect on a uniform flow behind wind-turbine model. *J. Phys. Conf. Ser.* **2015**, *625*, 012011. [CrossRef]

29. Stein, V.P.; Kaltenbach, H.J. Non-Equilibrium Scaling Applied to the Wake Evolution of a Model Scale Wind Turbine. *Energies* **2019**, *12*, 2763. [CrossRef]

30. Neunaber, I.; Obligado, M.; Peinke, J.; Aubrun, S. Application of the Townsend-George wake theory to field measurements of wind turbine wakes. *J. Phys. Conf. Ser.* **2021**, *934*, 012004. [CrossRef]

31. Neunaber, I.; Hölling, M.; Obligado, M. Leading effect for wind turbine wake models. *arXiv* **2022**, arXiv:2209.04935.

32. Barthelmie, R.J.; Hansen, K.; Frandsen, S.T.; Rathmann, O.; Schepers, J.G.; Schlez, W.; Phillips, J.; Rados, K.; Zervos, A.; Politis, E.S.; et al. Modelling and measuring flow and wind turbine wakes in large wind farms offshore. *Wind Energy* **2009**, *12*, 431–444. [CrossRef]

33. Townsend, A. The fully developed turbulent wake of a circular cylinder. *Aust. J. Chem.* **1949**, *2*, 451–468. [CrossRef]

34. Kolmogorov, A. Dissipation of energy in locally isotropic turbulence. *Dokl. Akad. Nauk SSSR* **1941**, *32*, 16.

35. Dairay, T.; Obligado, M.; Vassilicos, J. Non-equilibrium scaling laws in axisymmetric turbulent wakes. *J. Fluid Mech.* **2015**, *781*, 166–195. [CrossRef]

36. Obligado, M.; Dairay, T.; Vassilicos, J. Non-equilibrium scaling of turbulent wakes. *Phys. Rev. Fluids* **2016**, *1*, 044409. [CrossRef]

37. Nedic, J.; Vassilicos, J.; Ganapathisubramani, B. Axisymmetric Turbulent Wakes with New Nonequilibrium Similarity Scalings. *Phys. Rev. Lett.* **2013**, *111*, 144503. [CrossRef]

38. Blondel, F.; Cathelain, M. An alternative form of the super-Gaussian wind turbine wake model. *Wind Energy Sci.* **2020**, *5*, 1225–1236. [CrossRef]

39. Cafiero, G.; Obligado, M.; Vassilicos, J.C. Length scales in turbulent free shear flows. *J. Turbul.* **2020**, *21*, 243–257. [CrossRef]

40. Kröger, L.; Frederik, J.; van Wingerden, J.W.; Peinke, J.; Hölling, M. Generation of user defined turbulent inflow conditions by an active grid for validation experiments. *J. Phys. Conf. Ser.* **2018**, *1037*, 052002. [CrossRef]

41. Schottler, J.; Hölling, A.; Peinke, J.; Hölling, M. Design and implementation of a controllable model wind turbine for experimental studies. *J. Phys. Conf. Ser.* **2016**, *753*, 072030. [CrossRef]
42. Neunaber, I.; Hölling, M.; Whale, J.; Peinke, J. Comparison of the turbulence in the wakes of an actuator disc and a model wind turbine by higher order statistics: A wind tunnel study. *Renew. Energy* **2021**, *179*, 1650–1662. [CrossRef]
43. Schottler, J.; Bartl, J.; Mühle, F.; Sætran, L.; Peinke, J.; Hölling, M. Wind tunnel experiments on wind turbine wakes in yaw: Redefining the wake width. *Wind Energy Sci.* **2018**, *3*, 257–273. [CrossRef]
44. Abraham, A.; Martínez-Tossas, L.A.; Hong, J. Mechanisms of dynamic near-wake modulation of a utility-scale wind turbine. *J. Fluid Mech.* **2021**, *926*, A29. [CrossRef]
45. Mora, D.O.; Obligado, M. Estimating the integral length scale on turbulent flows from the zero crossings of the longitudinal velocity fluctuation. *Exp. Fluids* **2020**, *61*, 1–10. [CrossRef]
46. Pope, S.B.; Pope, S.B. *Turbulent flows*; Cambridge University Press: Cambridge, UK, 2000.